Ozone depletion during the solar proton events of October/November 2003 as seen by SCIAMACHY

G. Rohen,[1] C. von Savigny,[1] M. Sinnhuber,[1] E. J. Llewellyn,[2] J. W. Kaiser,[3] C. H. Jackman,[4] M.-B. Kallenrode,[5] J. Schröter,[5] K.-U. Eichmann,[1] H. Bovensmann,[1] and J. P. Burrows[1]

Received 17 December 2004; revised 4 May 2005; accepted 13 May 2005; published 20 August 2005.

[1] We use atmospheric ozone density profiles between 35 and 65 km altitude derived from SCIAMACHY limb measurements to quantify the ozone changes caused by the solar proton events from 26 October to 6 November 2003, known as the "Halloween storm." Detailed maps and daily resolved time series up to 5 weeks after the first event are compared with the results from a chemistry, transport, and photolysis model of the middle atmosphere that includes NO_x and HO_x production due to energetic particle precipitation. The general features of the ozone loss are captured by the model fairly well. A strong ozone depletion of more than 50% even deep into the stratosphere is observed at high geomagnetic latitudes in the Northern Hemisphere, whereas the observed ozone depletion in the more sunlit Southern Hemisphere is much weaker. Reasons for these interhemispheric differences are given. Two regimes can be distinguished, one above about 50 km dominated by HO_x (H, OH, HO_2) driven ozone loss, one below about 50 km, dominated by NO_x (NO, NO_2) driven ozone loss. The regimes display a different temporal evolution of ozone depletion and recovery. We observe for the first time an establishment of two contemporaneous maxima of ozone depletion at different altitudes, which solely can be explained by these regimes.

Citation: Rohen, G., et al. (2005), Ozone depletion during the solar proton events of October/November 2003 as seen by SCIAMACHY, *J. Geophys. Res.*, *110*, A09S39, doi:10.1029/2004JA010984.

1. Introduction

[2] The Sun drives the photochemistry of the atmosphere with variations of solar irradiation on different timescales, e.g., the 11 year solar cycle, that has been shown to cause variations in the total ozone column [*Jackman et al.*, 1996], the occurrence frequency and brightness of noctilucent clouds [*Thomas and Olivero*, 1989], and many other atmospheric parameters. The Sun also affects the terrestrial atmosphere through more intermittent events like coronal mass ejections that enhance the precipitation of highly energetic particles (protons, electrons, and ions) into the mesosphere and upper stratosphere [e.g., *Weeks et al.*, 1972; *Crutzen et al.*, 1975; *Baker*, 2000]. These charged particles do not penetrate the atmosphere at all latitudes but are supposed to be guided by the Earth's magnetic field lines and therefore enter the middle atmosphere in the polar cap regions mainly at geomagnetic latitudes above 60°.

[3] The penetration depth and the ion production rates are a function of the proton energies. Protons with energies of about 1 MeV reach the mesopause, 10 MeV protons reach about 65 km, and protons with 100 MeV get down to about 30–35 km [*Reid*, 1986].

[4] During a solar proton event (SPE) the incident highly energetic protons ionize the major atmospheric constituents N_2^+(58.5% partitioning of total ionization), N^+(18.5%), O^+(15.4%), and O_2^+ (7.6%) [*Solomon et al.*, 1981]. The transformation of all initial ions to intermediate water clusters [*Swider and Keneshea*, 1973; *Solomon et al.*, 1981; *Jackman and McPeters*, 2004], further clustering and dissociative recombination of these water clusters produce the main HO_x constituents H and OH.

[5] NO is a result of dissociation of N_2 and a series of interchange and recombination reactions involving nitrogen and its ions [*Rusch et al.*, 1981]. The net effect is the production of atomic nitrogen, which is oxidized to nitric oxide.

[6] Ozone is destroyed through the well-known HO_x and NO_x cycles. The HO_x catalytic cycle is very efficient in the mesosphere and upper stratosphere (above about 40 km), whereas the NO_x cycle is most efficient in the middle stratosphere [*Lary*, 1997; *Wayne*, 1985, p. 128ff.].

[7] To make the effect of the SPE induced ozone depletion clear, we recapitulate the sources and sinks of HO_x and

[1]Institute of Environmental Physics, University of Bremen, Bremen, Germany.
[2]Institute of Space and Atmospheric Studies, Department of Physics and Physics Engineering, University of Saskatchewan, Saskatoon, Saskatchewan, Canada.
[3]Remote Sensing Laboratories, Department of Geography, University of Zurich, Zurich, Switzerland.
[4]NASA Goddard Space Flight Center, Greenbelt, Maryland, USA.
[5]Physics Department, University of Osnabrück, Osnabrück, Germany.

0148-0227/05/2004JA010984$09.00

NO_x under normal conditions: HO_x is normally produced by photolysis of water vapor and reaction of atomic oxygen with water vapor and is quickly destroyed by itself through

$$OH + HO_2 \rightarrow H_2O + O_2. \quad (1)$$

The largest natural source of NO, the main driver of the NO_x cycle, is the reaction of nitrous oxide with atomic oxygen, which is produced by photolysis of ozone:

$$O + N_2O \rightarrow 2NO. \quad (2)$$

The depletion of NO again is due to photolysis

$$NO + h\nu \rightarrow N + O, \quad \nu < 191\ nm \quad (3)$$

or reaction with atomic nitrogen by

$$N + NO \rightarrow N_2 + O. \quad (4)$$

Owing to the optical thickness of the atmosphere for radiation at wavelengths below 191 nm, photolysis of NO is mainly active at altitudes above about 50 km.

[8] The ozone depletion through HO_x follows the ionization nearly instantaneously and is rapidly reduced again, after the enhanced proton fluxes cease [*Solomon et al.*, 1981]. In contrast, the NO_x induced depletion destroys ozone for several months up to years by conserved NO_x sinking down to the stratosphere [*Crutzen et al.*, 1975; *Randall et al.*, 2005].

[9] In the summer hemisphere the SPE induced depletion of ozone can be observed less clearly due to the already photolyzed water vapor and therefore more ambient HO_x. With continuous solar illumination and hence ozone production, the SPE depleted ozone can recover again quickly. Also, NO_x is depleted faster in the summer hemisphere (see equation (3)), which leads to an enhancement of ozone concentrations, too.

[10] Although the catalytic ozone destruction can reach 50% and more in the mesosphere and upper stratosphere, the impact on the total ozone column, and therefore on the UV-irradiance at the surface associated even with strong SPEs, is less than 1–2% [*Jackman et al.*, 2005a]. Apart from the production of HO_x and NO_x SPEs were also previously speculated to lead to an enhanced stratospheric aerosol loading caused by ion nucleation of sulphate aerosol particles [*Shumilov et al.*, 1996]. MIPAS observations [*Orsolini et al.*, 2005] showed an establishment of a high-altitude (35–45 km) HNO_3 layer between 20 November 2003 and early January 2004 that is induced by NO_x produced during the SPE in October/November 2003. HNO_3 is supposed to be photolyzed to yield OH in the upper stratosphere and mesosphere [*Solomon et al.*, 1981]. They also showed a confinement of these phenomena to the polar vortex regions.

[11] According to *Jackman et al.* [2005a], the 28/29 October SPE was the fourth largest SPE within the past 4 decades in terms of the total amount of NO_x produced (3.4×10^{33} molecules NO_x). The largest SPE ever measured occurred in October 1989 (6.7×10^{33} molecules NO_x), followed by the events on August 1972 (3.6×10^{33} molecules NO_x) and 14 July 2000 (3.5×10^{33} molecules NO_x). *Seppälä et al.* [2004] published the first results on ozone depletion and production of NO_2 due to the October/November 2003 SPEs retrieved from GOMOS (Global Ozone Monitoring by Occultation of Stars) on board the spacecraft Envisat. The study focuses on Northern Hemisphere (NH) observations during nighttime. *Seppälä et al.* [2004] presented zonally averaged ozone and nitrogen dioxide profiles at geographic latitudes in the NH between 70°N and 75°N and compared them with results from a non-SPE forcing model.

[12] The long-term effects of this SPE on NO_2 and O_3 concentrations between March and July 2004 as seen by numerous satellite instruments like MIPAS (Michelson Interferometer for Passive Atmospheric Sounding), HALOE (Halogen Occultation Experiment), SAGE III (Stratospheric Aerosol and Gas Experiment III), POAM III (Polar Ozone and Aerosol Measurement), and OSIRIS (Optical Spectrograph and Infrared Imager System) are shown in the work of *Randall et al.* [2005]. They showed that the NO_x enhancements and O_3 reductions from January 2004 up to July 2004 are attributed to a combination of the effects of the SPE event in October/November 2003 and an exceptionally strong vortex. HALOE and SBUV/2 (Solar Backscatter Ultraviolet Instrument, Version 2) satellite observations of O_3 and changes of NO_x (NO and NO_2) during the Halloween storm and model simulations of O_3, NO_x, and OH in both hemispheres are presented in the work of *Jackman et al.* [2005b]. *Jackman et al.* [2005b] predicted OH enhancements of 100% and measured ozone depletions of greater than 70% and a NO_x induced long-term ozone depletion for over 8 months past the SPE in October/November 2003.

[13] In this paper we use limb scatter measurements made with the SCIAMACHY (Scanning Imaging Absorption Spectrometer for Atmospheric Chartography) [*Bovensmann et al.*, 1999] instrument on the Envisat (Environmental Satellite) spacecraft of the European Space Agency (ESA) to retrieve ozone profiles in the mesosphere and upper stratosphere before, during, and up to 6 weeks after the series of SPEs in October/November 2003.

[14] A brief overview of the SCIAMACHY instrument is given in section 2. Since the mesospheric ozone retrievals are a new scientific data product, the retrieval algorithm, as well as an error budget are presented in section 3. The two-dimensional (2-D) photochemical model used to simulate the SPE induced ozone destruction is briefly described in section 4. The observations are presented, discussed, and compared to the model simulations in section 5, and final conclusions are drawn in section 6.

2. SCIAMACHY on Envisat

[15] SCIAMACHY is an 8-channel UV/Visible/NIR grating spectrometer covering the spectral range between 220 nm and 2380 nm with a channel-dependent spectral resolution between 0.25 nm and 1.5 nm. Apart from nadir-backscatter and solar/lunar occultation observations SCIAMACHY also measures limb scattered solar radiation. In limb-viewing mode the tangent height (TH) range from −3 to 92 km is stepped through in 3.3 km steps. An azimuthal

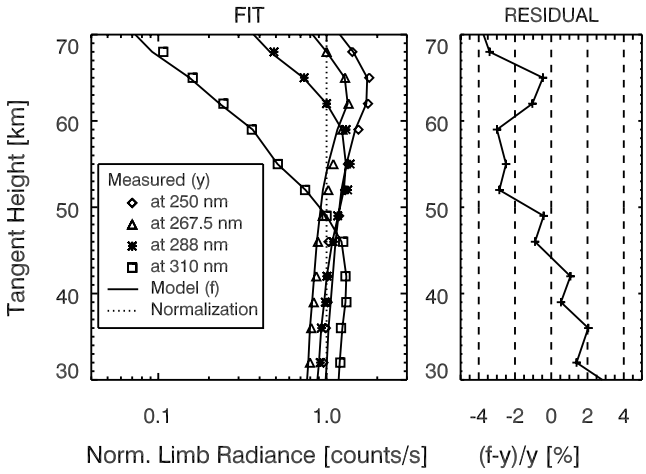

Figure 1. Fit of the normalized modeled limb radiance profiles and the sample measured limb radiance profiles for selected wavelengths (left). The right panel shows the averaged residual of the fit at 13 wavelengths. The measurement was made on 2 November, 2003 (67°N, 155°E, 68° solar zenith angle).

scan of 960 km is performed at each TH step. The instantaneous field of view in limb mode is 110 km horizontally and 2.6 km vertically. The spacecraft Envisat is in a polar Sun-synchronous orbit with an inclination angle of 98.7° and a descending node at 1000 local solar time (LST). More information on the SCIAMACHY instrument and its scientific objectives can be found in the work of *Bovensmann et al.* [1999, 2004].

3. Upper Stratospheric/Lower Mesospheric Ozone Profile Retrievals

3.1. Methodology

[16] The upper stratospheric/lower mesospheric ozone profile retrieval method [*Rohen et al.*, 2005] is similar to the one applied to Solar Mesosphere Explorer (SME) ultraviolet (UV) limb scattering satellite observations [*Rusch et al.*, 1984] and to the method used for stratospheric ozone profile retrievals from SCIAMACHY limb scattering observations [*von Savigny et al.*, 2005]. The method exploits the absorption of solar radiation in the ozone Hartley bands (~240–310 nm). The wavelengths are chosen to avoid Fraunhofer lines and terrestrial airglow emissions, e.g., the prominent NO γ-bands [*Rohen et al.*, 2005]. The wavelengths λ_i, (i = 1,...,13) are 250, 252, 254, 264, 267.5, 273, 283, 286, 288, 290.5, 305, 307, and 310 nm. In the first step the UV limb radiance profiles at these selected wavelengths $I_{i,k}$, (k = 1,...,31, k being the TH index) are normalized with respect to the limb radiance $I_{i,ref}$ at a certain wavelength dependent reference TH.

$$I_{i,k}^{norm} = \frac{I_{i,k}}{I_{i,ref}} \tag{5}$$

This normalization reduces systematic errors caused by technical and natural sources and the TH for the normalizations are chosen empirically slightly above the particular "knee" between 56 and 70 km. The retrieval is performed with a nonlinear optimal estimation (OE) scheme [*Rodgers*, 1976]

$$\mathbf{x}_{n+1} = \mathbf{x}_0 + \mathbf{S}_{x_0}\mathbf{K}_n^T\left(\mathbf{K}_n\mathbf{S}_{x_0}\mathbf{K}_n^T + \mathbf{S}_y\right)^{-1}((\mathbf{y} - \mathbf{y}_n) - \mathbf{K}_n(\mathbf{x}_0 - \mathbf{x}_n)), \tag{6}$$

where $\mathbf{x}_{n+1}$ corresponds to the logarithm of the ozone profile estimate after n + 1 iterations, $\mathbf{x}_0$ is the logarithm of the a priori ozone profile, $\mathbf{y}$ is the natural logarithm of the retrieval vector obtained from the SCIAMACHY limb measurement, i.e., the normalized limb radiance profiles $\mathbf{I}^{norm}$ in one vector in a wavelength-ascending order, and $\mathbf{y}_n$ is the logarithm of the modeled retrieval vector for the nth ozone profile estimate $\mathbf{x}_n$. The logarithm of all profiles in equation (6) is taken due to a better convergence of the iteration scheme.

[17] The weighting function matrix is given by $\mathbf{K}_n = \left.\frac{\partial \mathbf{y}}{\partial \mathbf{x}}\right|_{x_n}$. The weighting functions as well as the modeled retrieval vector are calculated with the spherical radiative transfer model SCIARAYS [*Kaiser and Burrows*, 2003]. The a priori covariance matrix $\mathbf{S}_{x_0}$ is assumed to be diagonal and the standard deviation for each altitude is assumed to be 65% of the a priori profile $\mathbf{x}_0$. The measurement covariance matrix $\mathbf{S}_y$ is also chosen to be diagonal with an estimated error of 8%. Furthermore, the temperature dependent ozone absorption cross sections of the GOME (Global Ozone Monitoring Experiment) flight model [*Burrows et al.*, 1999] are used.

[18] SCIARAYS is a spherical model considering two orders of scattering and surface reflection. Owing to massive absorption of solar radiation by ozone in the spectral range below 310 nm, the first order of scattering is sufficient for a precise profile retrieval. SCIARAYS allows for the semianalytical determination of the weighting functions [*Kaiser and Burrows*, 2003], which is significantly faster than the more conventional perturbation technique. Figure 1 shows an example of the normalized radiance profiles compared with fit results from SCIAMACHY limb scatter-

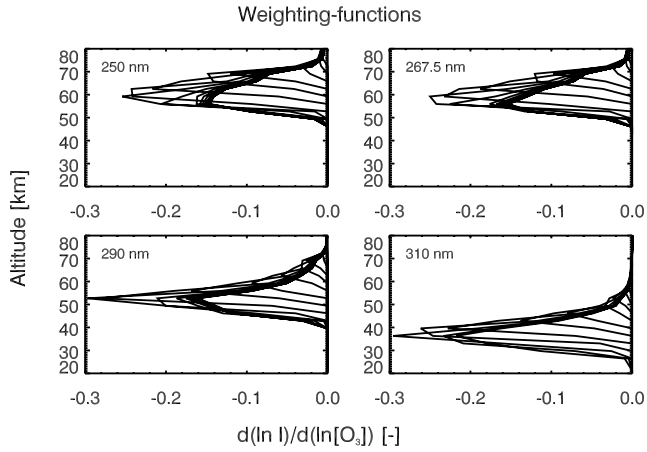

Figure 2. Weighting functions at four selected wavelengths for the profile retrieval shown in Figure 1. The altitude range, where the limb radiance profiles are sensitive to ozone, shifts with wavelengths.

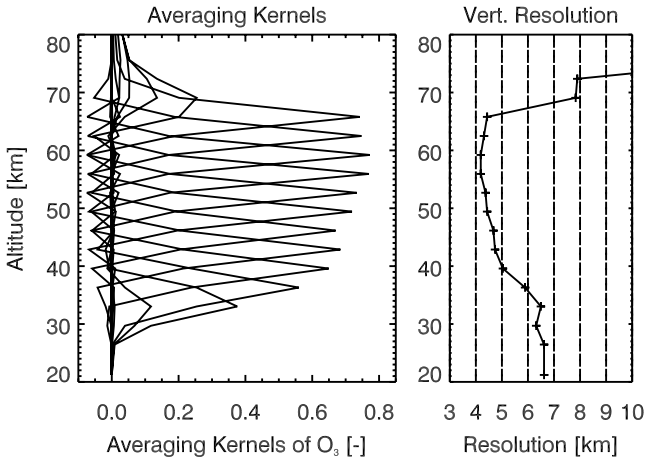

Figure 3. Averaging kernels for the sample profile retrieval shown in Figure 1 (left). The right panel shows the vertical resolution of the retrieved profiles as given by the FWHM (Full Width at Half Maximum) of the averaging kernel functions.

ing measurements for four selected wavelengths. Also shown is the averaged residual for all 13 wavelengths. The weighting functions at four selected wavelengths for this sample profile retrieval are shown in Figure 2. The shorter the wavelength, the higher are the altitudes, where the limb radiances are sensitive to ozone. This is due to the fact that down in the Hartley bands from 310 nm to 250 nm, the ozone absorption cross sections increase with decreasing wavelength. Therefore radiation at shorter wavelengths will already be absorbed higher up in the atmosphere. Averaging kernels of the sample profile retrieval are shown in Figure 3, indicating that the altitude range between about 35 and 70 km can be covered with the chosen wavelengths. In the right panel the full width at half maximum (FWHM) of the averaging kernel functions is shown, i.e., a measure for the vertical resolution of the profile retrieval method. Within the 40 to 65 km altitude range the vertical resolution is about 4–5 km.

[19] The background atmosphere climatology used for the profile retrieval is taken from *McPeters* [1993], and the a priori ozone profiles are taken from the monthly and latitudinally resolved Universities Global Atmospheric Modelling Programme (UGAMP) climatology [*Li and Shine*, 1995], which is based on 5-year averaged data of SME [*Rusch et al.*, 1983], Stratospheric Aerosol and Gas Experiment II (SAGE II) [*McCormick et al.*, 1989] and Solar Backscatter Ultraviolet (SBUV) [*Fleig et al.*, 1990].

3.2. Error Budget

[20] The method to retrieve mesospheric ozone concentrations is essentially based on the shape of the limb radiance profiles in the ozone Hartley bands. Therefore any other parameter or process affecting the limb radiance profiles is a potential error source and its effect has to be estimated. A series of sensitivity studies was performed to establish an error budget, and an overview of the most important sources of error is given in Table 1.

[21] The impact of the ground albedo on the retrieved ozone concentrations is basically negligible. This is a consequence of the absorption of radiation in the Hartley bands of ozone. Here solar photons have a very small probability to reach the surface and then get transmitted to the line of sight and get scattered into the field of view of the spectrometer. Another consequence of the absorption is the rare occurrence of multiple scattering. In the upper stratosphere for wavelengths below about 310 nm an error of less than 3% occurs by neglecting multiple-scattering and less than 0.3% in the lower mesosphere [*Rohen et al.*, 2005]. Since multiple-scattering is negligible, profile retrievals with single-scattering forward models are sufficient. Furthermore, the model calculations are very fast. Another advantage of using the Hartley bands is their weaker temperature dependence compared with the Huggins bands. This minimizes the errors caused by the temperature climatology profiles.

[22] The most important source of error within the 40–65 km altitude range originates from pointing errors. The Envisat TH information is affected by errors of up to 3 km for measurements during the SPE (C. von Savigny et al., Spatial and temporal characterization of SCIAMACHY limb pointing errors during the first three years of the mission, submitted to *Atmospheric Chemistry and Physics*, 2005, hereinafter referred to as von Savigny et al., submitted manuscript, 2005). These TH errors can be traced back to incorrect knowledge of the spacecraft's attitude and/or position. In order to correct for the TH errors the TRUE (Tangent Height Retrieval by UV-B Exploitation) [*Kaiser et al.*, 2004] pointing retrieval method was implemented. The TRUE method is based on a generalization of the "knee" method [*Janz et al.*, 1996; *Sioris et al.*, 2003]. The "knee" refers to a maximum in the UV-B limb radiance profile in the upper stratosphere caused by the absorption of solar radiation in the Hartley bands of ozone (see the "knee" in Figure 1). For all limb measurements used a pointing retrieval is performed prior to the retrieval of ozone profiles as described in the work of von Savigny et al. (submitted manuscript, 2005). The TH retrievals have an error of about 500 m, leading to profile errors of up to 19% (see Table 1).

[23] In limb-viewing mode, SCIAMACHY scans the atmosphere at a tangent point that is about 3300 km away from the subsatellite point. This ensures partly that the satellite measurements in the auroral oval are not affected

Table 1. Summary of the Sensitivity Studies Where the Errors of the Retrieved Profiles for Different Altitudes Between 35 and 65 km Are Listed in Percentages

	Errors of the Retrieved Profiles					
Altitude, km	35	39	45	51	57	65
Single-scattering[a]	3.0	1.0	0.3	0.1	0.1	0.1
A priori[b]	12.0	1.0	3.0	2.5	3.0	7.0
Ground albedo (A)[c]	2.0	0.6	0.1	0.1	0.1	0.1
Background density[d]	0.7	1.2	0.7	0.2	0.1	0.1
Temperature[e]	10.0	7.0	3.0	2.0	1.0	3.0
Pointing errors[f]	4.0	10.0	15.0	16.0	17.5	19.0
Cross sections[g]	4.0	7.0	5.0	2.0	1.0	2.0

[a]Neglecting second scattering order and reflection.
[b]Change of 100%.
[c]Changing from A = 0 to A = 0.5.
[d]20% decrease.
[e]$\Delta T = 40$ K.
[f]$\Delta h = 0.5$ km.
[g]$\Delta T = 40$ K.

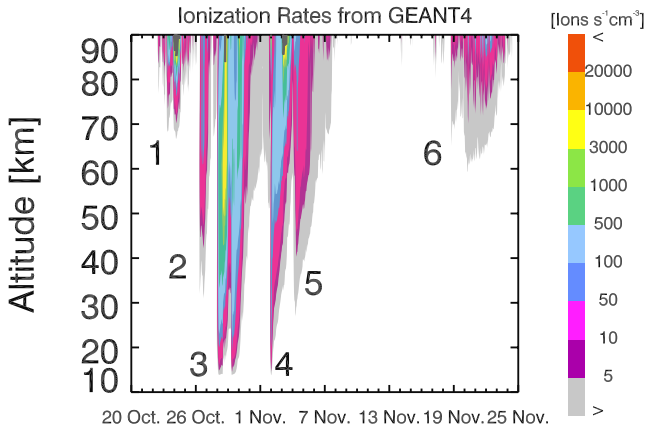

Figure 4. Atmospheric ionization rate profiles from the GEANT4 toolkit in the northern hemisphere. Hourly resolved rates are used for the photochemical calculations. The marks on the abscissa denote 0000 UTC of the particular day. The vertical resolution is about 3.5 km.

by radiation and particle hits, in particular during solar proton events. Investigations of the limb spectra profiles at magnetic latitudes above 60° in the NH and Southern Hemisphere (SH) showed no indications of radiation hits affecting the retrievals. This is caused partly by the large extent of the spacecraft Envisat, which acts like a protection shield and partly due to the fact, that only discrete wavelengths are used instead of a continuous spectral range with more detector pixels. Thus for better coverage, even measurements with subsatellite points inside the magnetic polar cap are used.

[24] The estimated total retrieval error of the ozone profiles within the altitude range from 35 to 65 km is generally less than 20%. This estimate is consistent with first validation results using 434 geographically coinciding ozone profiles, measured in March 2004 with the Michelson Interferometer for Passive Atmospheric Sounding (MIPAS) (profile retrieval version V4.61) on Envisat, showing agreement to within 15% [*Rohen et al.*, 2005].

4. Modeling Ionization and the Impact of SPEs on Chemical Composition

[25] The effect of highly energetic solar protons on the chemical composition of the middle atmosphere is modeled in two steps. In the first step atmospheric ionization rates are calculated from measured proton fluxes. In the second step those ionization rates are used in a photochemical model of the neutral atmosphere.

4.1. Atmospheric Ionization

[26] Ionization rates for precipitating protons are calculated with a Monte-Carlo code based on the Gigabit European Academic Network 4 (GEANT4) toolkit [*Agostinelli et al.*, 2003]. First, the energy spectra of precipitating protons in the range from 1 to 500 MeV are retrieved from the Geostationary Operational Environmental Satellite 11 (GOES-11) data. These serve as input for a Monte Carlo simulation, which calculates energy losses for a standard atmosphere consisting of N, O, O_2, N_2, and Ar. Ion pair production rates are determined assuming an average ionization energy of 35 eV [*Porter et al.*, 1976]. The considered energy range is discretized in 109 equidistant energy steps on a logarithmic scale and the precipitation angles in nine equidistant steps from 0 to 80°. Both scales are logarithmic. Particle precipitation and subsequent ionization is assumed to occur homogeneously throughout the entire magnetic polar cap and the ionization rates are determined for precipitating protons only, since reliable electron data were not available.

[27] The error in ionization rates due to the neglect of the electrons are smaller than 10% on average. J. Schröter et al. (Energetic particles in the atmosphere: A Monte-Carlo simulation, submitted to *Advances in Space Research*, 2005) showed that the maximum partition of electrons to the total ionization at two solar flares in 1989 is located at 50–70 km altitude, never exceeds 30%, and is smaller than 10% on average. The partition depends strongly whether the event is gradual and electron-poor or impulsive and electron-rich [*Kallenrode et al.*, 1992]. Since the Halloween storm originated in a gradual flare and was accompanied by a strong shock, the event can be classified as electron-poor.

[28] Figure 4 shows the calculated ionization rates for the northern polar cap during the SPE in October/November 2003. The ionization of the atmosphere on 24–27 October (indicated by 1 in Figure 4) is associated with high ionization rates in the upper mesosphere and mesopause region but does not cause significant ionization below 70 km. On 27 October a first weak and short ionization (indicated by 2 in Figure 4) down to about 40 km follows. On 28 October the first major sustaining ionization of the middle atmosphere begins (indicated by 3 in Figure 4), reaches the lower stratosphere at about 15 km and lasts for several days. It is followed by two large ionization periods between 3 and 7 November (indicated by 4 and 5 in Figure 4). In the end a smaller event occurred between 20 November and 25 November down to 60 km (indicated by 6 in Figure 4). Ionization rates used by *Jackman et al.* [2005b] derived with the methodology as described by *Vitt and Jackman* [1996] agree with this calculated ionization rates almost exactly.

4.2. Photochemical Model

[29] To consider the geographic distribution and the variability of the solar zenith angles of the SCIAMACHY measurements, a combination of a 2-D chemistry transport model runs and of a 1-D model run is used. The chemistry codes of both models are based on the SLIMCAT code [*Chipperfield*, 1999]. The 2-D and 1-D models use the same number of reactions, the same reaction rates, and the same implementation of ionization driven NO_x and HO_x production. The 2-D model uses a time-saving family approach for short-lived species, while the 1-D model is used to model the diurnal variability of trace gases and does not use a family approach. The formation of NO_x and HO_x due to atmospheric ionization is calculated with an empirical algorithm based on *Porter et al.* [1976] and *Solomon et al.* [1981], and is similar to the approach of *Jackman et al.* [2005b]: 1.25 NO_x are produced per ion pair in total. 55% are produced as NO and 45% are produced as ground-state N, which can be a sink for NO_x via the reaction of N and NO. Up to two HO_x molecules are produced per ion pair,

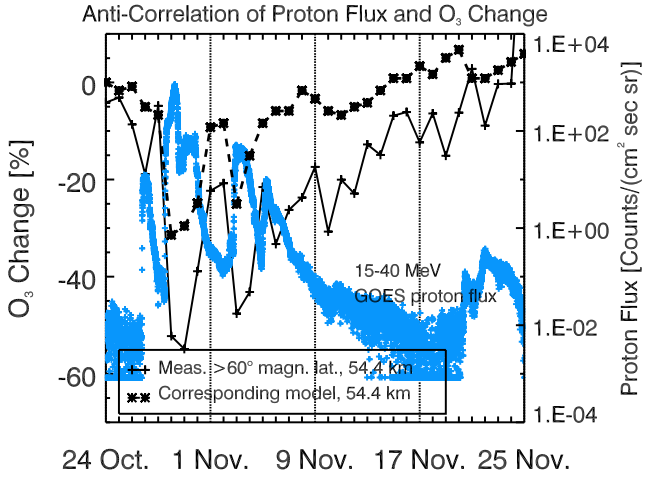

Figure 5. Ozone depletion rates above 60°N geomagnetic latitude (solid line), model results (stars) and GOES-11 15–40 MeV proton flux (blue points). The altitude is 54.4 km and the observation and model data are daily and zonally averaged. The reference period for this picture and for all following figures later in this paper is 20–24 October, 2003.

decreasing with increasing altitude and atmospheric ionization, as described by *Jackman et al* [2005b]. The 2-D model combines the chemistry code with the THIN AIR meteorological code [*Kinnersley*, 1996], which calculates temperature, pressure and wind speed on isentropic surfaces from the bottom up to 100 km. Vertical transport across the isentropes is calculated from heating rates. The model has a horizontal resolution of 9.5°, extending from 85.3°S–85.3°N in 19 evenly spaced latitude bands, and a vertical resolution of about 3 km. Twenty-four different model runs are carried out with the 2-D model on different longitude bands from the Greenwich meridian once around the globe in 15° steps. Ionization is considered in areas, where the geomagnetic latitude is larger than 60°. Different model runs for different longitudinal segments are necessary because of the large displacement of the southern geomagnetic polar cap. For model boxes containing the edge of the polar cap, ionization is scaled by the ratio of the polar cap area within this box to the total box area. This might lead to an unprecise estimation of the ionization effect in areas at the edge region of the polar cap, a possible error source that could only be avoided by drastically increasing the spatial resolution of the model boxes.

[30] Model results from the 2-D model are used to initialize a 1-D model run with the SZA of the distinct SCIAMACHY measurement. In the 1-D model, ionization is again considered for all measurements of magnetic latitude larger than 60°. The 1-D model runs are initialized 1 day before the measurement and run for 2 days. Model results are then read out at the time of the corresponding SCIAMACHY measurement.

5. Results and Discussion

5.1. Response to Proton Fluxes

[31] Figure 5 shows the time series of zonally averaged ozone changes at 54.4 km altitude in the NH above 60°N geomagnetic latitude from 23 October to 24 November 2003. Also depicted are model results and the GOES-11 proton flux with energies of 15–40 MeV, which are mainly responsible for the atmospheric ionization at this altitude [*Reid*, 1986]. The reference period for Figure 5 and all following figures in this paper is 20–24 October 2003.

[32] The proton flux and the ozone depletion rates at this altitude are mostly anticorrelated. Deviations of proton fluxes and the measured ozone depletion rates (e.g., on 1 November) can be explained by the sampling of the measurements. Model simulations reproduce the depletion qualitatively well but absolutely underestimate the observations by about 20–30%. This is most likely caused by incorrect ionization calculations and applications in the model and will be discussed later more comprehensively.

[33] The largest signatures occur on 28–30 October and on 3–4 November. On 10 November the measured ozone recovery is slowed down, which is obviously not caused by the proton precipitation directly but most likely by the sampling of the measurements. The variation of about 10% as seen in the measured ozone changes after 10 November is caused by errors most likely induced by the imprecise attitude pointing of Envisat (see discussion in section 3.2).

[34] The time series of ozone depletion rates agrees qualitatively fairly well with observations of GOMOS [*Seppälä et al.*, 2004] and SBUV/2 [*Jackman et al.*, 2005b]. They both noticed maximum depletion rates of up to 60% in the NH in the stratosphere at about 45 km, which will be shown later to be in agreement with observations shown in this paper.

5.2. Interhemispheric Differences

[35] Figure 6 shows the change of ozone concentration at 49 km altitude in both hemispheres relative to the reference period 20–24 October in a global view. In the NH changes from 29 October to 6 November relative to the reference period are shown. For the representation of the ozone changes in the SH the shorter time period 29–30 October is chosen. The depletion of ozone in the SH is shorter term than in the NH, so averaging many days together would dilute the observed loss.

[36] The ozone profiles for the reference period and the ozone profiles for the SPE time periods are interpolated onto a grid of 2.5° latitude and 10° longitude steps using a Delaunay triangulation. Also shown are isolines of different magnetic latitudes ϕ_{mag}. These are determined from the magnetic inclination I (i.e., the angle between the tangential plane and the magnetic field vector) for 2003 calculated with the WMM 2000 (World Magnetic Model) [*MacMillan and Quinn*, 2000] and using the relation $\phi_{mag} = \arctan(1/2 \tan I)$ [*Prölls*, 2003, p. 224ff.]. This relation for ϕ_{mag} provides a better representation than the standard magnetic coordinates based on a magnetic dipole field because near the polar cap the actual Earth's magnetic field is not well represented by a pure dipole field.

[37] The error of the ozone changes represented in Figure 6 differs from the error of the retrieved profiles as noted in section 3.2. The normalization of ozone concentrations with respect to the concentrations before the SPE reduces the systematic errors, since a large number of profiles is averaged by the Delaunay triangulation. On the

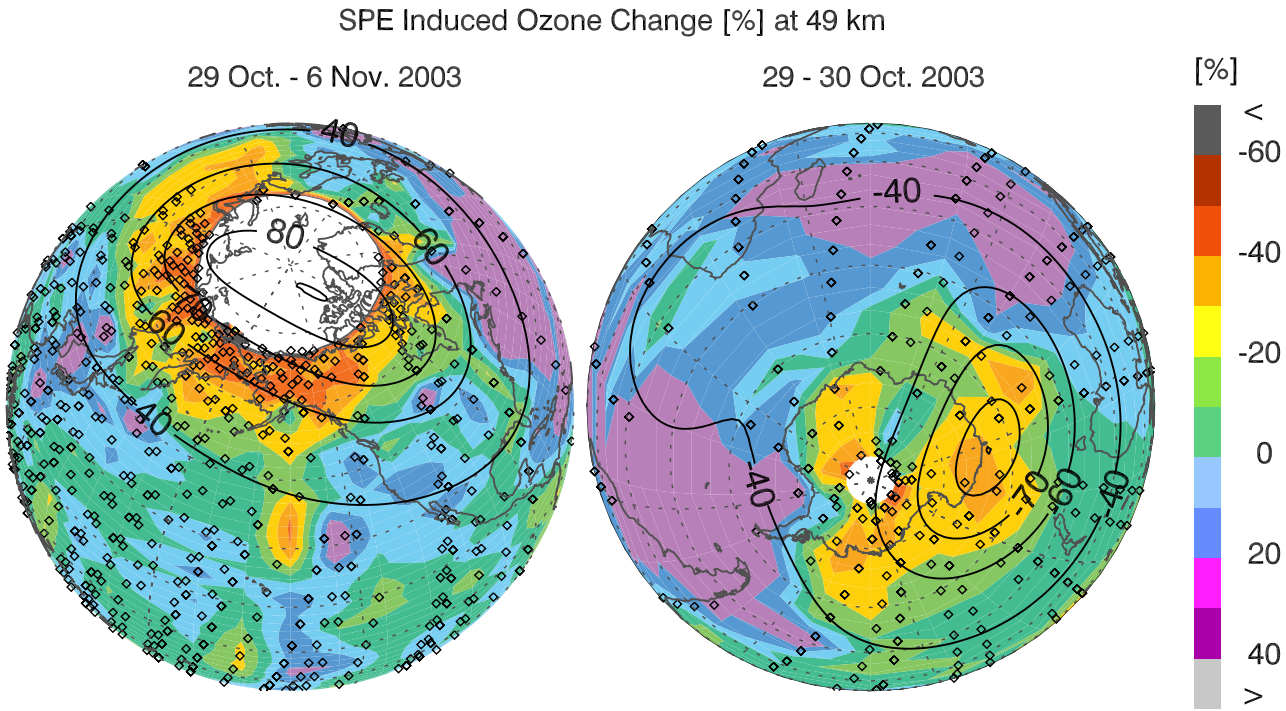

Figure 6. Change of ozone concentration at 49 km altitude in the NH and SH in a global view. Changes are shown for different time periods in each hemisphere, respectively. The reference period is 20–24 October 2003, like in all figures in this paper. Evidently the ozone depletion is confined to the geographic and geomagnetic poles. A Delaunay triangulation of the reference data set and the data set during the SPE and a following linear interpolation on a 2.5° latitude times 10° longitude grid is used. The white areas depict the places with no observations by the satellite. The open black diamonds indicate the tangent points of the limb measurements between 28 October and 5 November in the NH, measurements between 29 and 30 October in the SH, respectively. The black solid lines are the Earth's magnetic latitudes at 60 km altitude for 2003 derived with the WMM 2000 model [*MacMillan and Quinn*, 2000]. The Delaunay triangulation produces changes even at locations, where no measurements were taken, e.g., over Scandinavia. The error of the changes of about 20% can produce single anomalies in this representation, e.g., over Hawaii.

other hand, the maximum statistical error is larger by a factor $\sqrt{2}$. Therefore the maximum error of the changes is assumed to be larger than the error of the retrieved profiles.

[38] The SPEs cause ozone loss of several tens of percent in both hemispheres. In the NH the area of ozone depletion coincides generally more with the geographic polar cap than with the magnetic polar cap. The confinement to the polar vortex can also be seen in the long-term observations by *Randall et al.* [2005] and by *Orsolini et al.* [2005]. Perhaps strong winds cause a zonal mixing of the air masses at the edge of the vortex within the first week after the first event and are therefore the reason for the confinement of the ozone loss to the geographical pole. This discovery is new and still a puzzle.

[39] In the SH the ozone loss is mainly confined to the region with high magnetic latitudes. Additional depletion of ozone occurs around the geographic South Pole due to a larger SZA and therefore enhanced ozone depletion through photolysis and equation (2). An anomaly of the Earth's magnetic field is located above the South Atlantic, where ozone depletion is observed even outside the geographic polar cap. This depletion is in agreement with observations of *Jackman et al.* [2005b].

[40] The observed ozone depletion at 49 km differs significantly between the northern and the southern polar stratopause, as observed also by *Jackman et al.* [2005b]. In the NH maximum ozone depletion rates of 50% and more occur at 49 km. In contrast to that, the magnitude of the ozone depletion as well as the spatial extent is smaller in the sunlit SH. This is a consequence of smaller SZAs in the SH, i.e., stronger solar illumination, that leads to the photolysis of the ambient H_2O and higher ambient, not SPE-produced HO_x concentrations. Therefore the effect of the SPE-induced HO_x production is not as strong as in a dark hemisphere. Additionally, the SPE-depleted ozone in the SH recovers quickly with continuous solar illumination and photolysis of molecular oxygen for ozone production. NO_x is depleted faster through photolysis (see equation (3)) above about 50 km, which also intensifies the recovery of ozone. In contrast to that, in the winter hemisphere H_2O as well as NO are protected more from the sunlight and ozone can be depleted stronger and for a longer period of time.

[41] The observations of this interhemispheric difference, the shape of the ozone depletion area and the magnitude of the depletion rates agree fairly well with calculations of *Jackman et al.* [2005b]. *Seppälä et al.* [2004] provide

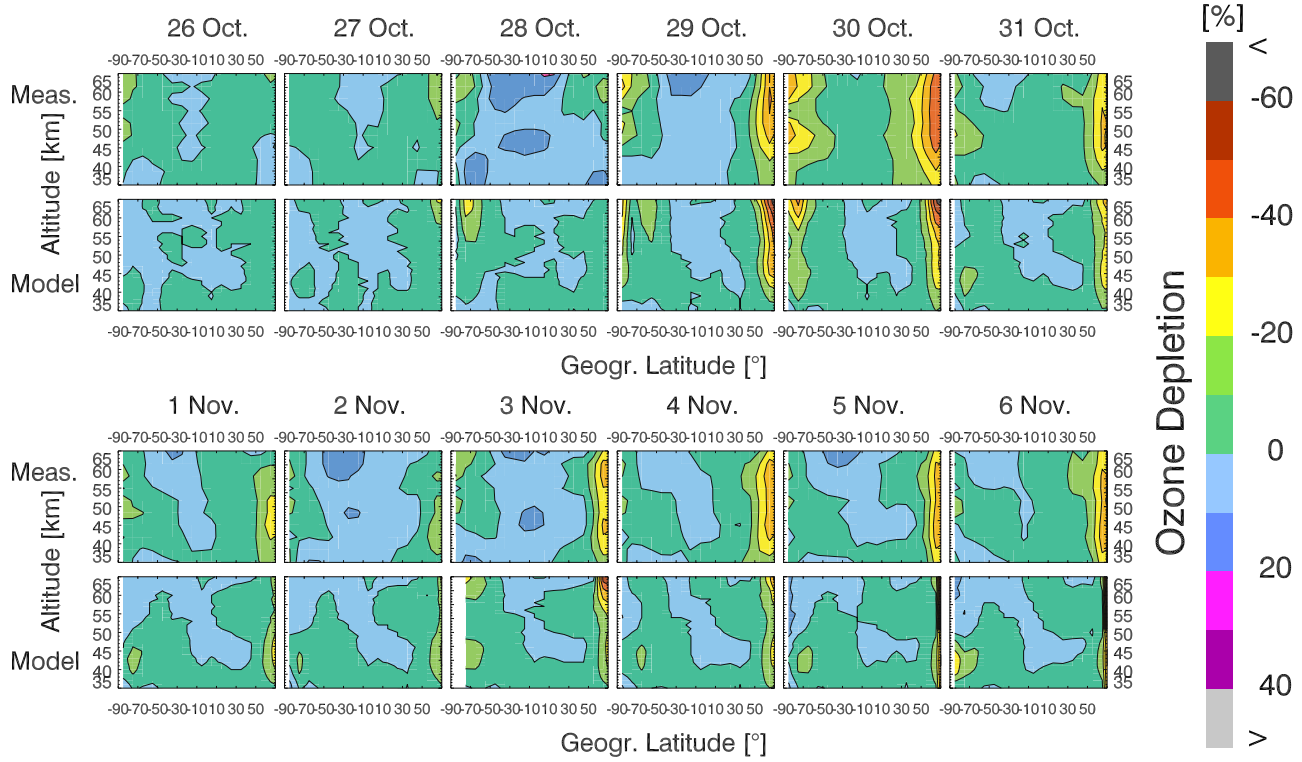

Figure 7. Measured and modeled change of ozone concentration during the SPE. Changes are represented as a function of geographic latitude. Measured and modeled data profiles are zonally averaged.

a very good comparison of the spatial extent of the ozone depletion area. They also found that the center of the depletion in the NH is located above Russia and North America. Above Europe, almost no depletion can be observed.

[42] SBUV observations of *Jackman et al.* [2005b] and the observations in this paper show that the ozone depletion in the SH is mainly located below Australia. Owing to the agreement of these measurements we can be sure of the correctness of the presentations shown in these papers.

5.3. Global Model Predictions

[43] Figure 7 shows the measured and modeled changes of ozone concentration before and during the SPE relative to the mentioned reference period 20–24 October for each day. The model runs predict the general morphology of ozone depletion and recovery fairly well, although the model slightly underestimates the ozone changes, as already seen in Figure 5. On 29 October the model overestimates the depletion dramatically. A separation of the ozone depletion on 3 November at about 50 km is observed, indicating the regimes of HO_x and NO_x. In the SH the model predicts the temporally varying morphology of the ozone depletion fairly well again. Only isolated ozone changes at about 70°S differ from the measurements.

[44] The general underestimation may be caused mainly by incorrect ionization rates due to calculation of the ionization rates itself or due to the transfer of these rates onto a geographical grid for the model calculations (see section 4.2). Further possible reasons for the underestimation may be the omission of the ionization by the solar electrons or simply by the fact that the spatial distribution of the calculated ionization used in the model is not as homogeneous as assumed.

[45] The overestimation on 29 October is due to the fact that in the model the production of HO_x due to ionization is calculated with empirical algorithms. Here the amount of available water vapor is not limited, which is in particular important during events with large HO_x production. Although HO_x is not present to that extent in the atmosphere, the model predicts much more HO_x. The isolated ozone changes in the SH at about 70°S are caused by the noncongruence of the southern geographic and magnetic pole, which leads to incorrect ionization rates at the edge of the auroral oval.

[46] Previous model runs showed that using only zonally averaged ionization rate profiles is insufficient for modeling the SPE effect, in particular in the SH, where the magnetic polar cap is not congruent with the geographic polar cap. Therefore we introduced longitudinal bins, improving the model results significantly. Differences between zonally averaged and longitudinally binned model results at the edge of the auroral oval were absolutely higher than 50%.

5.3.1. Ozone Depletion Time Series

[47] Figure 8 shows time series of ozone concentration changes between 24 October and 27 November in both hemispheres in the magnetic pole areas. The ozone depletion in the SH is weaker than in the NH, where the ozone depletion during the first large event on 28–30 October exceeds 50%. The second large event produces ozone depletion with two maxima at 45 and 55 km. These maxima can be seen again in the model results and in the SH

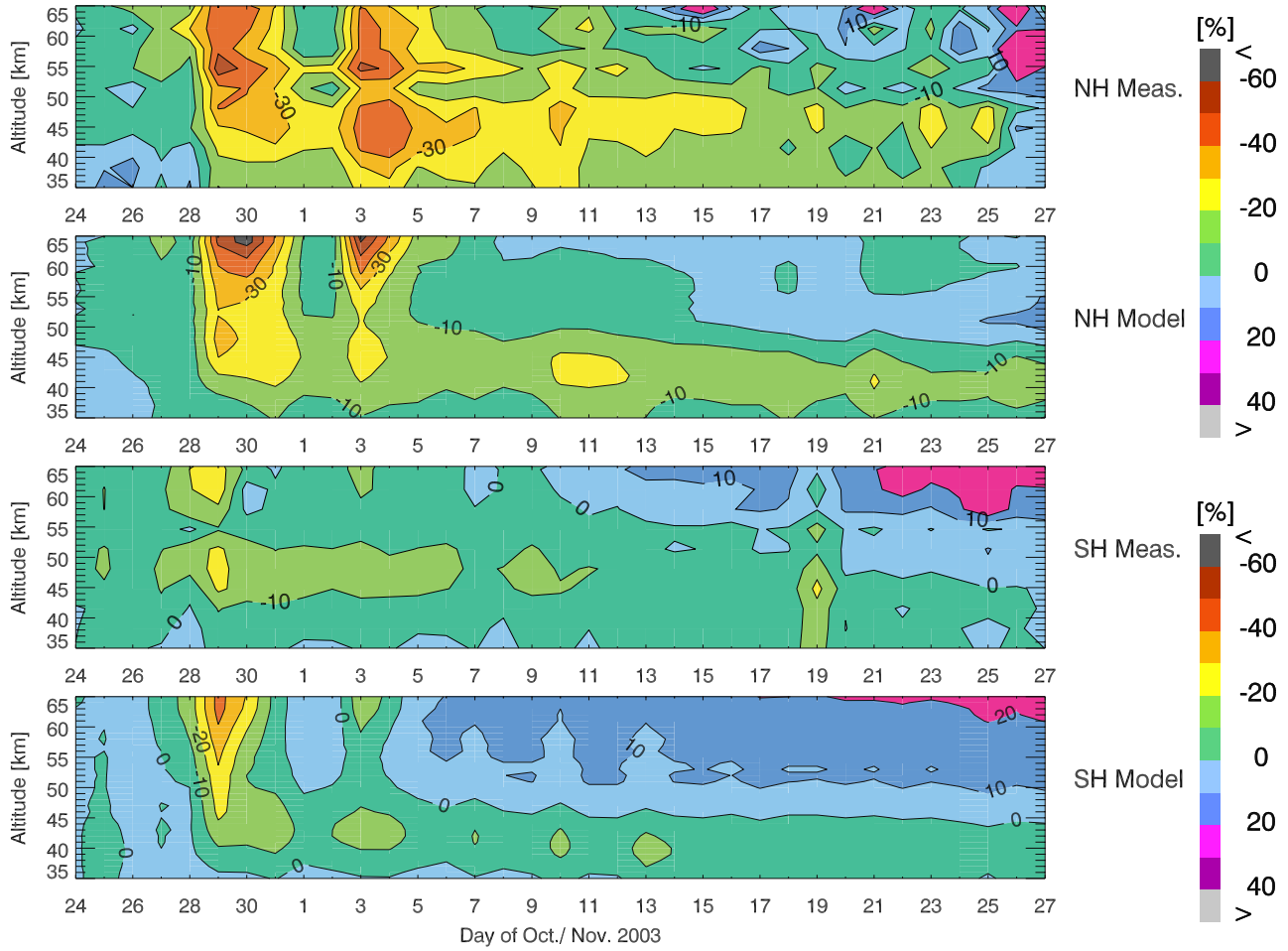

Figure 8. Ozone changes in both hemispheres above 60° magnetic latitude. Below each representation of the measurements the corresponding model results are shown. Retrieved profiles and model results are daily and zonally averaged.

measurements during the first event. After the second large event ozone recovers quickly above 50 km in both hemispheres, whereas below 50 km an ozone loss of about 10% continues for several weeks after the events.

[48] The interhemispheric difference is well captured by the model, as well as the fast recovery of ozone at higher altitudes due to the short lifetime of HO_x and photolytical reproduction of ozone. At lower altitudes the recovery of ozone is captured by the model well, too. The model also shows the regime change at about 50 km between ozone loss driven by short-lived HO_x and driven by long-lived NO_x. The modeled long-term ozone recovery is only slightly faster than in the observations. This is most likely again due to underestimated ionization rates (see section 4.2 and 5.3).

[49] The establishment of the two maxima is due to the fact that in the NO_x regime between 35 and 50 km [*Rusch et al.*, 1981] ozone recovers slower. Above 50 km ozone recovers quickly due to removed HO_x (equation (1)). Therefore in the NO_x regime an additional depletion of ozone by the event on 3–5 November leads to significantly lower absolute ozone concentrations. The second maximum above 55 km is due to higher ionization rates at higher altitudes. In the SH the model does not show these maxima

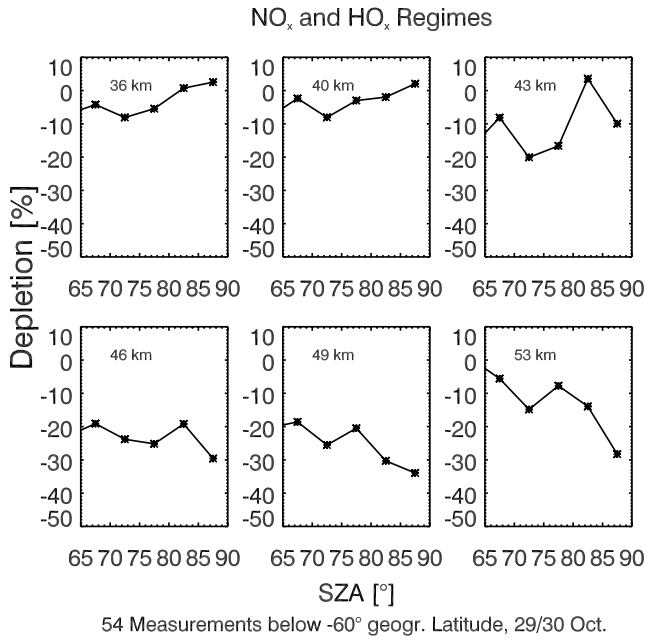

Figure 9. Ozone change on 29–30 October above 70°S geomagnetic latitude as a function of the SZA. Averaged measurements are shown from 36 km to 63 km.

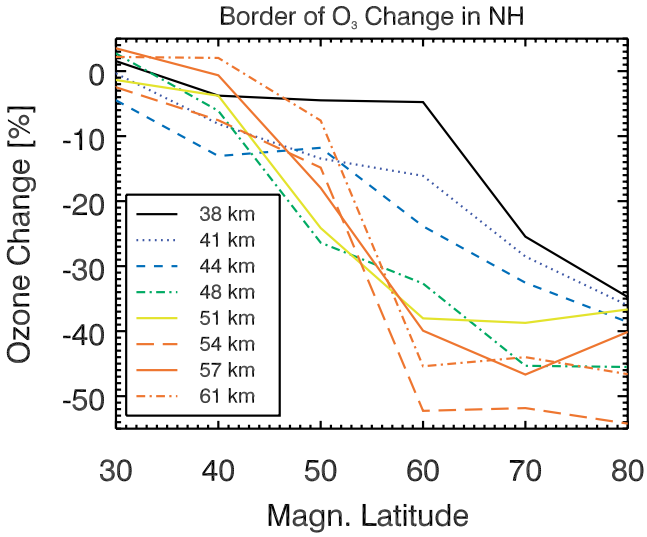

Figure 10. Ozone depletion rates at distinct altitudes in the NH on 29 and 30 October across the border of the auroral oval. Averages of the ozone changes within 10° latitude bins have been taken.

most likely due to the incorrect HO_x production during large events as discussed in the prior section.

[50] Additionally, an enhancement of ozone can be observed in both hemispheres above 45 km on 26 November in the NH and on 22–27 November in the SH. This was also seen by *Seppälä et al.* [2004] and is a seasonal effect.

5.4. HO_x and NO_x Regimes

[51] It has been shown in the work of *Solomon et al.* [1983] that in a HO_x dominated regime and for a horizontally homogeneous proton precipitation, the SPE induced ozone change is stronger at larger SZAs. This is due to the fact that at higher SZAs the SPE induced HO_x production is stronger relative to the HO_x production by H_2O photolysis before the SPE [*Solomon et al.*, 1981]. In contrast to that, the NO_x induced ozone loss is relatively large at low SZA. The NO_x catalytic cycle is more efficient due to enhanced production of atomic oxygen by photolysis (see equation (2)).

[52] Figure 9 shows the change of measured ozone concentrations on 29–30 October above 70°S geomagnetic latitude as a function of the SZA at different altitudes. At lower altitudes and small SZA ozone is mainly depleted by NO_x. With increasing SZA less ozone is depleted during the SPE. At higher altitudes more ozone is depleted with increasing SZA during the SPE.

[53] The dependence of the ozone depletion on the SZA can not be separated from the dependence on the magnetic latitude. Although this weakens the expressiveness of Figure 9, the dependence on the geomagnetic latitude can not explain the different behavior of the ozone change at different altitudes.

5.5. Vertical and Horizontal Extent of the Polar Cap Ozone Depletion

[54] The model calculations presume a vertical edge of the ionization at 60° magnetic latitude. Incorrect assumptions of the shape of the ionization area are a potential error source for modeling the ion chemistry. In Figure 10 ozone losses are shown across the border of the auroral oval. Ozone losses are not significant at low geomagnetic latitudes. They increase in a certain geomagnetic latitude range and stay more or less constant at high geomagnetic latitudes. At higher altitudes the transition from low to high ozone change occurs in a relatively small geomagnetic area around 50–60°N geomagnetic latitude. With decreasing altitudes, the transition region gets larger and the transition is less sharp. At lower altitudes ozone losses already occur at geomagnetic latitudes of 40–50°N.

[55] Although these findings can not be evaluated quantitatively because of the correlation of magnetic latitude and the SZA, significant ozone depletion is found even at geomagnetic latitudes between 40°N and 50°N. Neither vertical transport of NO_x can be a reason due to the slow vertical motion of the air masses, nor the gyroradii of the incident protons, which increase at lower altitudes only up to about 1000 km. The most likely reason is that the edge of the ionization is not as sharp as assumed in most of the models.

6. Conclusions

[56] SCIAMACHY limb measurements and a chemistry, transport, and photolysis model of the middle atmosphere that include NO_x and HO_x production due to energetic particle precipitation were used to study the effect of the October/November 2003 solar proton events on the atmospheric ozone concentrations between 35 and 65 km altitude until end of November 2003. We showed the vertical and spatial extent of the ozone depletion by detailed global maps and altitude resolved time series during 5 weeks after the first event in both hemispheres. In the Northern Hemisphere ozone was depleted up to 30% in the middle stratosphere and by up to 50% in the lower mesosphere. Interhemispheric differences were observed and reasons for this have been found. The effects of the HO_x and NO_x dominated regimes and their separation at about 50 km have been observed and discussed. We found two contemporaneous maxima of depletion at different altitudes, which have never been observed before and are caused by the catalytic ozone loss by HO_x and NO_x.

[57] The model predicted the general morphology of the ozone depletion and recovery of the changes fairly well. We showed that meridionally binned ionization rates are required for getting precise model results, in particular in the Southern Hemisphere.

[58] Additionally, we showed the correlation of the ozone depletion with magnetic coordinates. The shape of the border of the ozone depletion at low magnetic latitudes between 40°N and 50°N indicated that the assumption that ionization only occurs above 60°N magnetic latitude is not entirely correct, in particular in the stratosphere.

[59] **Acknowledgments.** This work was in part supported by the German Ministry of Education and Research BMBF (grant 07UFE12/8), the German Aerospace Center DLR (grant 50EE0027), the University of Bremen, and through grants-in-aid from the Natural Sciences and Engineering Research Council (NSERC) of Canada. We thank the European Space Agency for providing the SCIAMACHY data used in this study. Furthermore, we are indebted to all members of the SCIAMACHY team, whose efforts make all data analysis possible. Some of the retrievals shown

here were performed at the HLRN (High Performance Computing Center North). The HLRN service and support is gratefully acknowledged.

[60] Arthur Richmond thanks the reviewers for their assistance in evaluating this paper.

References

Agostinelli, S., et al. (2003), GEANT4 - a simulation toolkit, *Nucl. Instrum. Methods Phys. Res.*, *506*(3), 250–303.

Baker, D. N. (2000), Effects of the Sun on the Earth's environment, *J. Atmos. Sol. Terr. Phys.*, *62*, 1669–1691.

Bovensmann, H., et al. (1999), SCIAMACHY: Mission objectives and measurement modes, *J. Atmos. Sci.*, *56*(2), 127–150.

Bovensmann, H. et al. (2004), SCIAMACHY on ENVISAT: In-flight optical performance and first results, in *Remote Sensing of Clouds and the Atmosphere VIII*, *Proc. of SPIE*, vol. 5235, edited by K. P. Schäfer et al., pp. 160–173, SPIE, Bellingham, Wash.

Burrows, J. P., A. Richter, A. Dehn, B. Deters, S. Himmelmann, S. Voigt, and J. Orphal (1999), Atmospheric remote-sensing reference data from GOME: 2. Temperature-dependent absorption cross sections of O_3 in the 231–794 nm range, *J. Quant. Spectrosc. Radiat. Transfer*, *61*, 509–517.

Chipperfield, M. P. (1999), Multiannual simulations with a three-dimensional chemical transport model, *J. Geophys. Res.*, *104*, 1781–1805.

Crutzen, P. J., I. S. A. Isaksen, and G. C. Reid (1975), Solar proton events: Stratospheric sources of nitric oxide, *Science*, *189*, 457–458.

Fleig, A., R. McPeters, P. K. Barthia, B. Schlesinger, R. Cebula, K. Klenk, S. Taylor, and D. Heath (1990), Nimbus 7 Solar Backscatter Ultraviolet (SBUV) ozone products user's guide, *Ref. Publ. 1234*, NASA, Washington, D. C.

Jackman, C. H., and R. D. McPeters (2004), The effect of solar proton events on ozone and other constituents, in *Solar Variability and its Effects on Climate*, *Geophys. Monograph Ser.*, vol. 141, edited by J. M. Pap and P. Fox, pp. 305–319, AGU, Washington DC.

Jackman, C. H., E. L. Fleming, S. Chandra, D. B. Considine, and J. E. Rosenfield (1996), Past, present and future modeled ozone trends with comparisons to observed trends, *J. Geophys. Res.*, *101*, 28,753–28,767.

Jackman, C. H., M. T. DeLand, G. J. Labow, E. L. Fleming, D. K. Weisenstein, M. K. W. Ko, M. Sinnhuber, J. Anderson, and J. M. Russell (2005a), The influence of several very large solar proton events in years 2000–2003 on the neutral middle atmosphere, *Adv. Space Res.*, *35*, 445–450.

Jackman, C. H., M. T. DeLand, G. J. Labow, E. L. Fleming, D. K. Weisenstein, M. K. W. Ko, M. Sinnhuber, J. Anderson, and J. Russell (2005b), Neutral atmospheric influences of the solar proton events in October–November 2003, *J. Geophys. Res.*, *110*, A09S27, doi:10.1029/2004JA010888.

Janz, S. J., E. Hilsenrath, D. Flittner, and D. Heath (1996), Rayleigh scattering attitude sensor, *Proc. SPIE*, *2931*, 146–153.

Kaiser, J. W., and J. P. Burrows (2003), Fast weighting functions for retrievals from limb scattering measurements, *J. Quant. Spectrosc. Radiat. Transfer*, *77*, 273–283.

Kaiser, J. W., C. von Savigny, K.-U. Eichmann, S. Noël, H. Bovensmann, and J. P. Burrows (2004), Satellite-pointing retrieval from atmospheric limb-scattering of solar UV-B radiation, *Can. J. Phys.*, *82*, 1041–1052.

Kallenrode, M.-B., E. Cliver, and G. Wibberenz (1992), Composition and azimuthal spread of energetic particles from impulsive and gradual flares, *Astrophys. J.*, *391*, 370–379.

Kinnersley, J. S. (1996), The climatology of the stratospheric THIN AIR model, *Q. J. R. Meteorol. Soc.*, *122*, 219–252.

Lary, D. (1997), Catalytic destruction of stratospheric ozone, *J. Geophys. Res.*, *102*, 21,515–21,526.

Li, D., and K. P. Shine (1995), A 4-dimensional ozone climatology of ozone for UGAMP models, *UGAMP Int. Rep. 35*, British Geol. Survey, Dep. of Meteorol., Univ. of Reading, Reading, UK.

MacMillan, S., and J. M. Quinn (2000), The derivation of World Magnetic Model 2000, *Tech. Rep. WM/00/17R*, p. 278ff, British Geol. Survey, London.

McCormick, M. P., J. P. Zawodny, J. C. Larsen, and P. H. Wang (1989), An overview of SAGE I and II ozone measurements, *Planet. Space Sci.*, *37*(12), 1567–1586.

McPeters, R. (1993), Ozone profile comparisons. In: The atmospheric effects of stratospheric aircraft: Report of the 1992 models and measurement workshop, *Ref. Publ. 1292*, edited by M. J. Prather and E. E. Remsberg, pp. D31–D37, NASA, Washington, D. C.

Orsolini, Y. J., G. L. Manney, M. L. Santee, and C. E. Randall (2005), An upper stratospheric layer of enhanced HNO_3 following exceptional solar storms, *Geophys. Res. Lett.*, *32*, L12S01, doi:10.1029/2004GL021588.

Porter, H. S., C. H. Jackman, and A. E. S. Green (1976), Efficiencies for production of atomic nitrogen and oxygen by relativistic proton impact in air, *J. Chem. Phys.*, *65*, 154–167.

Prölls, G. W. (2003), *Physik des Erdnahen Weltraums*, Springer, New York.

Randall, C. E., et al. (2005), Stratospheric effects of energetic particle precipitation in 2003–2004, *Geophys. Res. Lett.*, *32*, L05802, doi:10.1029/2004GL022003.

Reid, G. C. (1986), Solar energetic particles and their effects on the terrestrial environment, in *Physics of the Sun*, vol. 3, edited by P. A. Sturrrock, pp. 251–278, chap. 12, Springer, New York.

Rodgers, C. D. (1976), Retrieval of atmospheric temperature and composition from remote measurements of thermal radiation, *Rev. Geophys.*, *14*, 609–624.

Rohen, G. J., C. von Savigny, E. J. Llewellyn, J. W. Kaiser, K.-U. Eichmann, A. Bracher, H. Bovensmann, and J. P. Burrows (2005), Upper stratospheric/lower mesospheric ozone profiles retrieved from SCIAMACHY limb spectra: Theory, error statistics, first validation and ozone depletion during the solar proton event in Oct./Nov. 2003, *Adv. Space Res.*, in press.

Rusch, D. W., J.-C. Gerard, S. Solomon, P. J. Crutzen, and G. C. Reid (1981), The effect of particle precipitation events on the neutral and ion chemistry of the middle atmosphere - I. Odd nitrogen, *Planet. Space Sci.*, *29*, 767–774.

Rusch, D. W., G. H. Mount, C. A. Barth, G. J. Rottman, R. J. Thomas, G. E. Thomas, R. W. Sanders, G. M. Lawrence, and R. S. Eckman (1983), Ozone densities in the lower mesosphere measured by a limb scanning UltraViolet Spectrometer, *Geophys. Res. Lett.*, *10*, 241–244.

Rusch, D. W., G. H. Mount, C. A. Barth, R. J. Thomas, and M. T. Callan (1984), Solar Mesosphere Explorer Ultraviolet Spectrometer: Measurements of ozone in the 1.0–0.1 mbar region, *J. Geophys. Res.*, *89*, 11,677–11,678.

Seppälä, A., P. T. Veronnen, E. Kyrölä, S. Hassinen, L. Backman, A. Hauchecorne, J. L. Bertaux, and D. Fussen (2004), Solar proton events of October–November 2003: Ozone depletion in the northern hemisphere polar winter as seen by GOMOS/Envisat, *Geophys. Res. Lett.*, *31*, L19107, doi:10.1029/2004GL021042.

Shumilov, O. I., E. A. Kasatkina, K. Henriksen, and E. V. Vashenyuk (1996), Enhancements of stratospheric aerosols after solar proton event, *Ann. Geophys.*, *14*, 1119–1123.

Sioris, C. E., et al. (2003), Stratospheric profiles of nitrogen dioxide observed by OSIRIS on the Odin satellite, *J. Geophys. Res.*, *108*(D7), 4215, doi:10.1029/2002JD002672.

Solomon, S., D. W. Rusch, J.-C. Gerard, G. C. Reid, and P. J. Crutzen (1981), The effect of particle precipitation events on the neutral and ion chemistry of the middle atmosphere: II. Odd hydrogen, *Planet. Space Sci.*, *29*(8), 885–892.

Solomon, S., G. C. Reid, D. W. Rusch, and R. J. Thomas (1983), Mesospheric ozone depletion during the solar proton event of July 13, 1982: 2. Comparison between theory and measurements, *Geophys. Res. Lett.*, *10*, 257–260.

Swider, W., and T. J. Keneshea (1973), Decrease of ozone and atomic oxygen in the lower mesosphere during a PCA event, *Planet. Space Sci.*, *21*, 1969–1973.

Thomas, G. E., and J. J. Olivero (1989), Climatology of polar mesospheric clouds: 2. Further analysis of Solar Mesosphere Explorer data, *J. Geophys. Res.*, *94*, 14,673–14,681.

Vitt, F. M., and C. H. Jackman (1996), A comparison of sources of odd nitrogen production from 1974 through 1993 in the Earth's middle atmosphere as calculated using a two-dimensional model, *J. Geophys. Res.*, *101*, 6729–6739.

von Savigny, C., et al. (2005), The ozone-hole break-up in September 2002 as seen by SCIAMACHY on Envisat, *J. Atmos. Sci.*, *62*(3), 721–734.

Wayne, R. P. (1985), *Chemistry of the Atmospheres*, 2nd ed., Oxford Univ. Press, New York.

Weeks, L. H., R. S. Cuikay, and J. R. Corbin (1972), Ozone measurements in the mesosphere during the solar proton event of 2 November 1969, *J. Atmos. Sci.*, *29*, 1138–1142.

H. Bovensmann, J. P. Burrows, K.-U. Eichmann, G. Rohen, M. Sinnhuber, and C. von Savigny, Institute of Environmental Physics, University of Bremen, Otto-Hahn-Allee 1, D-28359 Bremen, Germany. (rohen@iup.physik.uni-bremen.de)

C. H. Jackman, NASA Goddard Space Flight Center, Code 613.3, Greenbelt, MD 20771, USA.

J. W. Kaiser, Remote Sensing Laboratories, Department of Geography, University of Zurich, Winterthurer Str. 190, CH-8057 Zurich, Switzerland.

M.-B. Kallenrode and J. Schröter, Physics Department, University of Osnabrück, Barbarastr. 7, D-49076 Osnabrück, Germany.

E. J. Llewellyn, Institute of Space and Atmospheric Studies, Department of Physics and Physics Engineering, University of Saskatchewan, 116 Science Place, Saskatoon, Saskatchewan, S7N 5E2, Canada.